Eddy Transport of Heat and Thermocline Waters in the North Pacific: A Key to Interannual/Decadal Climate Variability?

DEAN ROEMMICH AND JOHN GILSON

Scripps Institution of Oceanography, University of California, San Diego, La Jolla, California

(Manuscript received 25 June 1999, in final form 9 May 2000)

ABSTRACT

High-resolution XBT transects in the North Pacific Ocean, at an average latitude of 22°N, are analyzed together with TOPEX/Poseidon altimetric data to determine the structure and transport characteristics of the mesoscale eddy field. Based on anomalies in dynamic height, 410 eddies are identified in 30 transects from 1991 to 1999, including eddies seen in multiple transects over a year or longer. Their wavelength is typically 500 km, with peak-to-trough temperature difference of 2.2°C in the center of the thermocline. The features slant westward with decreasing depth, by 0.8° of longitude on average from 400 m up to the sea surface. This tilt produces a depth-varying velocity/temperature correlation and hence a vertical meridional overturning circulation. In the mean, 3.9 Sv (Sv $\equiv 10^6$ m^3 s^{-1}) of thermocline waters are carried southward by the eddy field over the width of the basin, balanced mainly by northward flow in the surface layer. Corresponding northward heat transport is 0.086 $\pm$ 0.012 pW. The eddy field has considerable variability on seasonal to interannual timescales. For the 8-yr period studied here, eddy variability was the dominant mechanism for interannual change in the equatorward transport of thermocline waters, suggesting a potentially important forcing mechanism in the coupled air–sea climate system.

1. Introduction

This work focuses on the contribution of mesoscale eddies to the net meridional transport of water masses and heat in the North Pacific Ocean and on the potential role of this transport in the climate system. The role of eddies in large-scale ocean circulation and transport is a long-standing and observationally challenging topic. Point measurements have identified significant contributions of eddy fluxes (e.g., Niiler and Hall 1988; Wunsch 1999), but of uncertain spatial and temporal representativeness. It is the integral contribution of eddies over thousands of kilometers in space and years in time that defines their role in the climate system.

Investigations of the role of eddies in large-scale transport face prodigious sampling requirements. Most basin-scale subsurface datasets either do not resolve eddies, or if eddy-resolving, are not repeating in time to allow statistical analysis. The former of these includes the broadscale XBT data analyzed by Bennett and White (1986), and the latter includes many one-time hydrographic transects. Satellite altimetric data sample space and time domains very well, providing global observations of the surface displacement due to eddies (Stammer 1998). However, it is crucial to sample the vertical structure of eddies that gives rise to net transport.

For the present work, we use a subsurface dataset that is designed for basin-scale eddy-resolving studies. It spans length scales from tens of kilometers to the width of the Pacific. Thirty realizations of a high-resolution XBT transect, 12 700 km in length from San Francisco to Taiwan, have been collected over a period of eight years. These include temperature profiles at 10–50 km spacing. By one definition, the dataset includes 410 moderate to strong eddies at all longitudes of the tropical/subtropical North Pacific. The combination of this dataset with TOPEX/Poseidon (T/P) satellite altimetry spans a broad spectrum of spatial and temporal scales in sea surface and subsurface domains.

The eddies make a substantial but not dominant contribution to meridional heat transport in the North Pacific. Not surprisingly, meridional heat transport is mainly due to the large-scale heat engine of the subtropical gyre (Bryden et al. 1991). What is surprising is that the mesoscale features appear to be a major contributor to time variability in the basin-integrated southward transport of thermocline water masses.

This finding implies that the eddy generation mechanism in the region—baroclinic instability (Qiu 1999)—might be a causal factor in climate variability. The study area is near the tropical/subtropical boundary of the North Pacific, which has been identified as a possible

Corresponding author address: Dr. Dean Roemmich, Scripps Institution of Oceanography, University of California, San Diego, La Jolla, CA 92093-0230.
E-mail: droemmich@ucsd.edu

source of decadal-scale climate variability through thermocline advection. Decadal thermocline temperature anomalies are observed to propagate equatorward in the North Pacific (Deser et al. 1996). Model studies indicate that equatorward advection of anomalies may affect the equatorial thermocline (e.g., Gu and Philander 1997) and hence, via equatorial upwelling, air–sea feedbacks in low latitudes. If eddy processes are fundamental to time variability of equatorward thermocline transport, then not only does this set a difficult standard for resolution in observations and models, it also points to a potentially important source of climate forcing.

2. Eddies in XBT and altimetric data

The subsurface dataset consists of 30 XBT/XCTD transects collected from S/S *Sea–Land Enterprise* along a route from San Francisco to Honolulu to Guam to Taiwan (Fig. 1). In mid-1999, the Asian port was changed to Hong Kong, altering the westernmost segment of the track. A scientist or technician rides the ship four times per year in order to obtain closely spaced XBT profiles and sparse XCTDs. Over 300 XBT profiles, to about 800-m depth, are collected on each voyage (Fig. 2) as well as about 18 XCTD profiles. Probe spacing is $\frac{1}{2}^\circ$ of longitude in the ocean interior east of Guam. It decreases to $\frac{1}{3}^\circ$ west of Guam and can be $\frac{1}{10}^\circ$ or even finer in the Kuroshio and near sloping boundaries. Sampling began in late 1991 and continues to the present. The dataset includes 30 cruises through the end of 1999 and over 10 000 total XBT profiles. The transect and processing methods are described by Gilson et al. (1998). The route is part of a Pacific-wide network of high-resolution XBT/XCTD transects (Sprintall et al. 1996).

A typical XBT transect (Fig. 2) contains about 14 features that can be characterized as moderate to large mesoscale eddies. Their horizontal extent is several degrees of longitude. Eddy temperature anomalies on depth surfaces may be either warm or cold, in nearly equal numbers, with warm-to-cold contrast of 2°C or more in the thermocline. Isotherm displacements are vertically coherent through the thermocline, sometimes from the sea surface to the base of XBT profiles at about 800 m.

We will not try to distinguish between isolated eddies and wavelike sequences of warm and cold anomalies. In most cases, the temperature anomalies appear more wavelike. Alternating warm and cold anomalies are apparent even in unfiltered data (Fig. 2). Hence, usage of the word eddy is inclusive of individual mesoscale features and wavelike sequences.

Eddies are identified from their signature in dynamic height anomaly. After removing a basinwide mean and trend from each transect, the dynamic height field is Fourier decomposed. It is then bandpass filtered by omitting wavelengths shorter than 309 km (3.0° of longitude) and longer than 1002 km (9.7° of longitude)

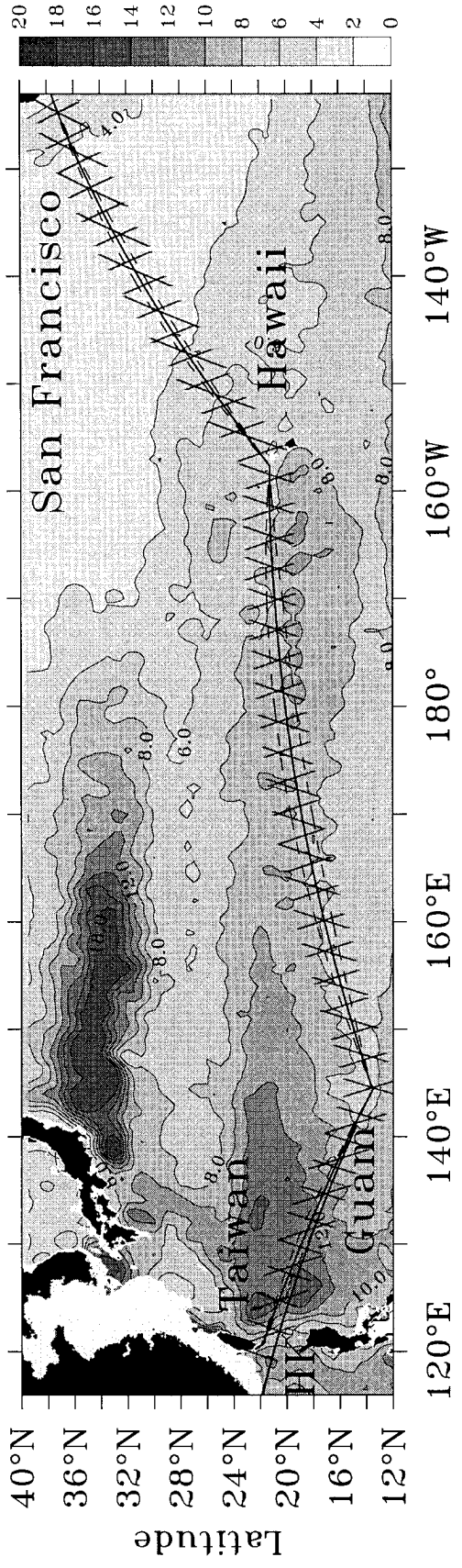

FIG. 1. Ship track of the S/S *Sea–Land Enterprise* from San Francisco to Taiwan, together with nearby *T/P* altimetric tracks. The *Enterprise* deviates very little, as shown by the dashed envelope (standard deviation), around the average track. In 1999, the ship's Asian port was changed to Hong Kong (HK). The contoured background is the rms variability of sea level (cm) from T/P data, high-pass filtered with an 8° lat by 20° long running mean.

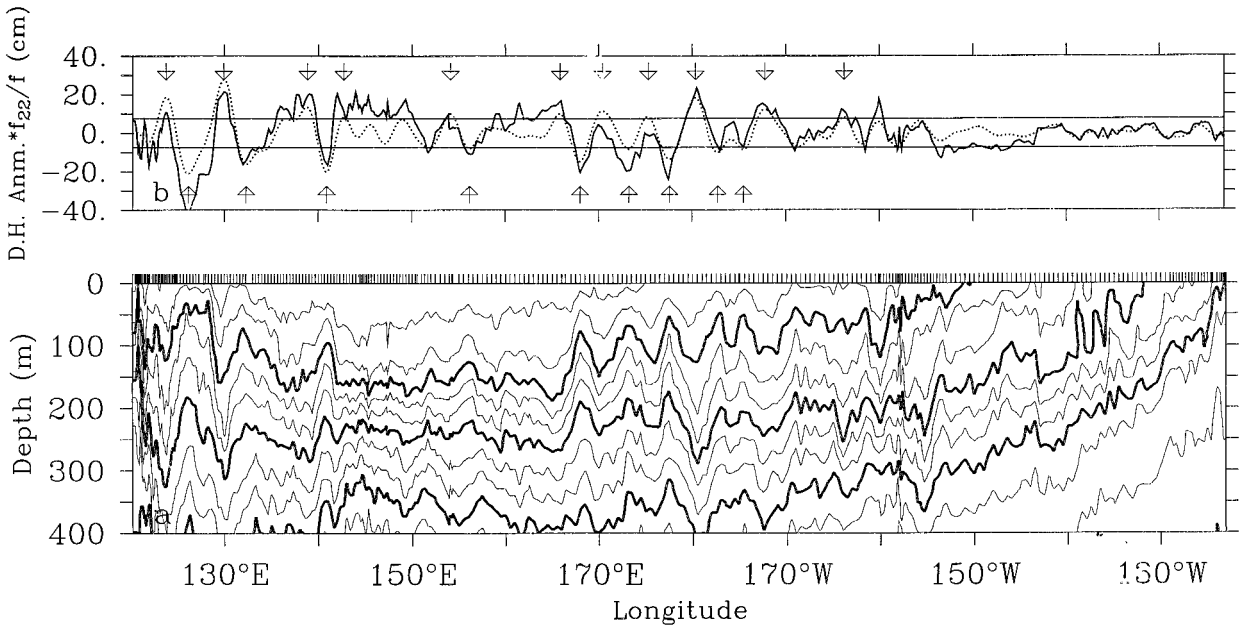

FIG. 2. A temperature section from a single transect in May 1996. The upper panel shows unfiltered (but detrended, solid) and bandpass filtered (dotted) dynamic height (0/800 m), scaled by latitude. Eddy locations are indicated by arrows.

from the reconstructed series. Equivalent distances (km) along the ship track are provided although longitude was selected as the natural basis for the Fourier decomposition (i.e., assuming zonal periodicity). The bandpass filter removes basin-scale signals, including most of the seasonal variability, in order to isolate mesoscale anomalies. The cutoff wavelengths are chosen by using the spectral analysis to isolate the vertically coherent band responsible for heat and water mass transport (sections 3 and 5, below). An alternate technique is to apply a 2000-km running mean filter to the raw dynamic height fields. This produces similar results to the Fourier method of identifying eddy locations.

In the bandpass filtered dynamic height, an eddy is defined as having a threshold anomaly of at least 7.5 dyn cm at 22°N. In order to select eddies of equivalent geostrophic transport, the 7.5 dyn cm threshold is applied to dynamic height scaled by latitude (dyn ht $\times$ f_{22}/f, where f_{22} is the Coriolis parameter at 22°N). In Fig. 2, arrows indicate locations identified as eddy centers by this criterion. The 7.5-cm threshold is chosen so that the automated eddy identification procedure agrees with our visual selection of moderate to large eddies. To that extent the threshold is subjective, but we will show below that strong and weaker eddies have similar size and vertical tilt.

In order to compare eddies in the XBT dynamic height field with features seen in the T/P altimetric data, T/P data were interpolated onto the ship track (Fig. 1) at 10-day intervals (Gilson et al. 1998). The interpolated dataset is missing some small-scale variance because of the separation of T/P tracks, but larger eddies and eddies near T/P tracks are captured. The same eddy identification process was used with T/P data as with XBT data. A 7.5-cm latitude-normalized height criterion was applied to the bandpass filtered T/P series.

Figure 3 shows eddy locations identified independently in the T/P and XBT datasets. The coincidence of features in the two datasets is remarkable. The T/P dataset allows individual eddies in the XBT cruises to be clearly tracked for a year or longer. In that time, they move thousands of kilometers to the west at about 10 cm s^{-1}. It is the diagonal nature of the ship track (Fig. 1) toward Guam and Taiwan that limits the ability to follow individual features even farther westward. A separate map of T/P height along constant latitude of 22°N (not shown) demonstrates that individual features can be tracked continuously from near Hawaii to the western boundary. In Fig. 3, the decrease in eddies near 150°E is clearly associated with the southward dip of the ship track toward Guam, away from the eddy-rich latitudes near 20°N (Fig. 1).

The alongtrack and temporal variability of eddies is illustrated in Fig. 4. The XBT and T/P datasets show nearly equal numbers of eddies in each 10° longitude bin (Fig. 4a). They both have maxima in the number of eddies near the date line and the western boundary. Minima are found in the eastern (northern) bins and in the bin containing Guam (the southernmost). There is good agreement between the spatial distribution in the number of eddies (Fig. 4b) and the sea surface height variability (Fig. 1). A time series of the number of eddies per transect (Fig. 4b) shows variability on a range of temporal scales. The T/P dataset has as few as 3 eddies at a given time and as many as 23. The second half of

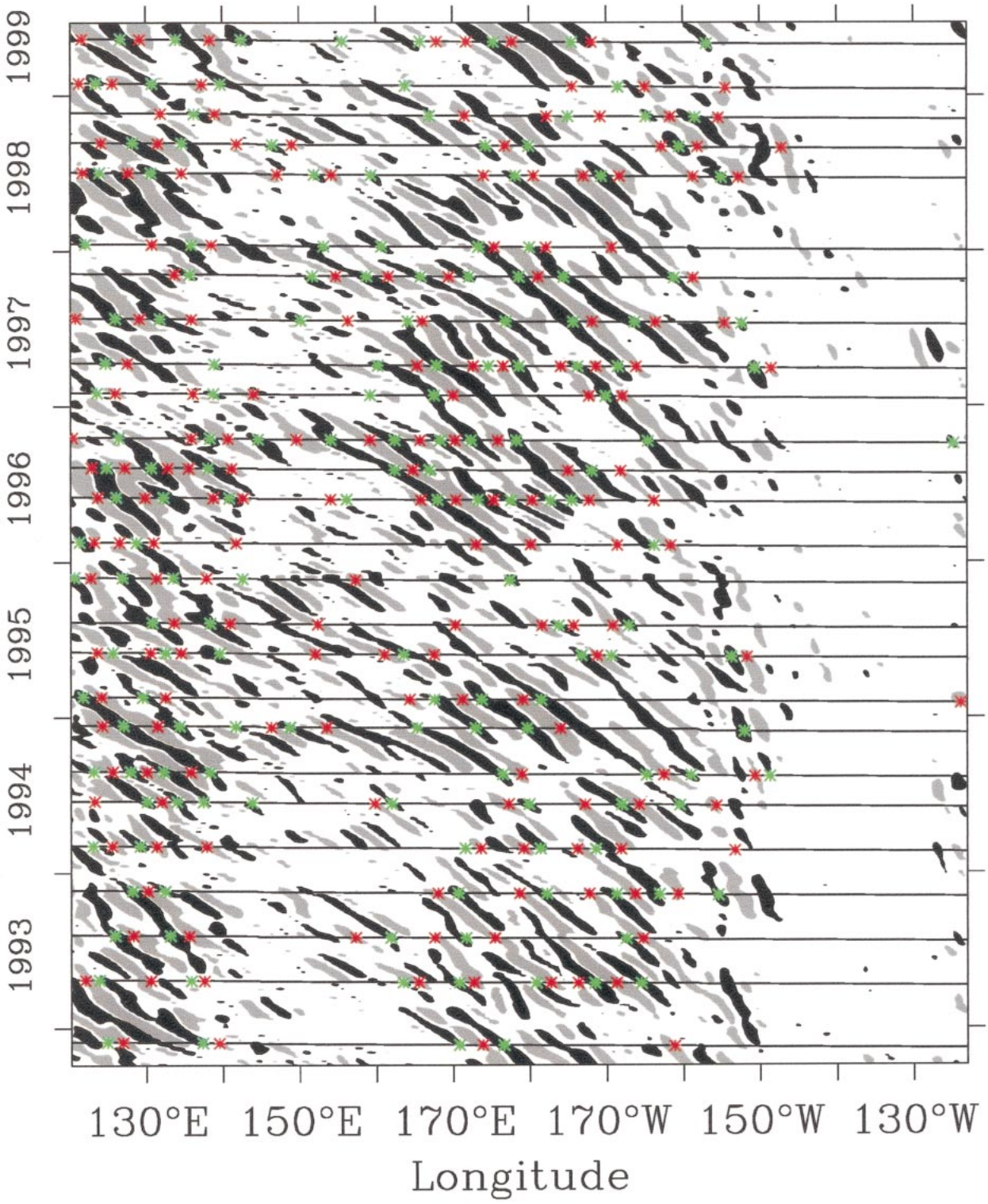

FIG. 3. Eddy locations in T/P and XBT data as a function of longitude and time. Warm (cold) core eddies with sea surface height maxima (minima) are shown as red (green) symbols for XBT data and gray (black) shading for T/P data.

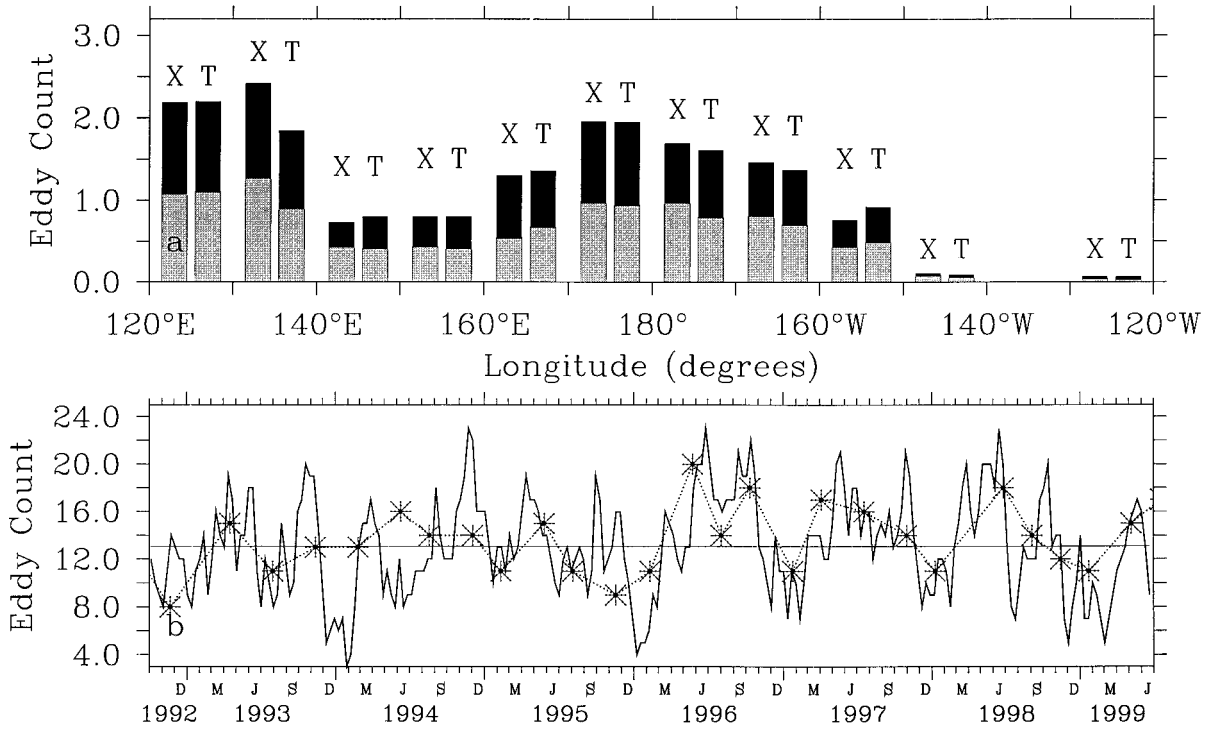

FIG. 4. (a) Census of eddies in longitude bins. For each 10° bin, the left-hand bar (labeled ×) shows the average number of warm (gray) and cold (black) core eddies from the XBT transects. The right-hand bar of each pair (labeled T) shows the corresponding average numbers from T/P data. (b) Time series of eddies per transect (all longitudes) in XBT (symbols, dotted line) and T/P (solid) data. The horizontal line is the mean value (13.1) for T/P data.

the T/P record has more eddies at a given time (13.8) than the first half (12.3).

The ''eddies'' identified in Fig. 3 are the same features described by Chelton and Schlax (1996) as Rossby waves. They have the same westward propagation speed of about 10 cm s^{-1} at 20°N and they dominate the space–time covariance structure of sea surface height (e.g., Gilson et al. 1998, their Fig. 3). That the same features are observed in both altimetry and XBT transects makes the combination of the datasets very powerful. The XBT data can be used to describe the subsurface thermal structure, as detailed in the next section, while the altimetric data provide excellent spatial and temporal sampling of surface height.

3. The composite eddy

After identifying eddy locations in bandpass filtered dynamic height, a composite eddy was constructed. Temperature fields from all transects were bandpass filtered, applying the same filter cutoffs at each depth as for the dynamic height. Eddies within 5° of the eastern and western boundaries were excluded, limiting the total number to 372–192 warm core and 180 cold core eddies. For averaging purposes, the features were divided into sets of warm and cold core eddies. The eddies of each group were aligned using the location of their central maximum or minimum in dynamic height. Figure 5 shows the mean temperature, the temperature anomaly (with respect to the mean at each depth), and the geostrophic velocity for the warm and cold composite eddy. Clearly, the warm and cold core composites are very similar in size, shape, and magnitude. Composites of unfiltered data are also similar.

The width of either composite eddy, from one sidelobe to the other, is about 4.7° of longitude (485 km along the ship track). This width is consistent with an estimate based on the zero crossing of the T/P alongtrack autocorrelation function (Stammer 1998). The maximum temperature anomaly in the composite eddy is found at 160 m depth, where the core temperature anomaly is 2.2°C warmer (or colder) than at the sidelobes. This temperature contrast drops to 0.8°C at 400 m. The dynamic height signature of the eddy is 14.7 dyn cm higher (or lower) at the maximum than at the sidelobes.

A notable characteristic of either composite eddy is the westward tilt of the eddy toward the sea surface, by about 0.8° of longitude in the upper 400 m. XBT profiles are at ½° intervals over much of the ocean, and at ⅓° or ¼° intervals in the western ocean, where the strongest eddies occur. The phase shift with depth is robust with respect to averaging over warm or cold core eddies (Fig. 5) or over subsets of cruises, and can also be seen in composites from different portions of the transect. The reversal of the tilt below 400 m is also a robust feature, but its effects are less noticeable because the associated

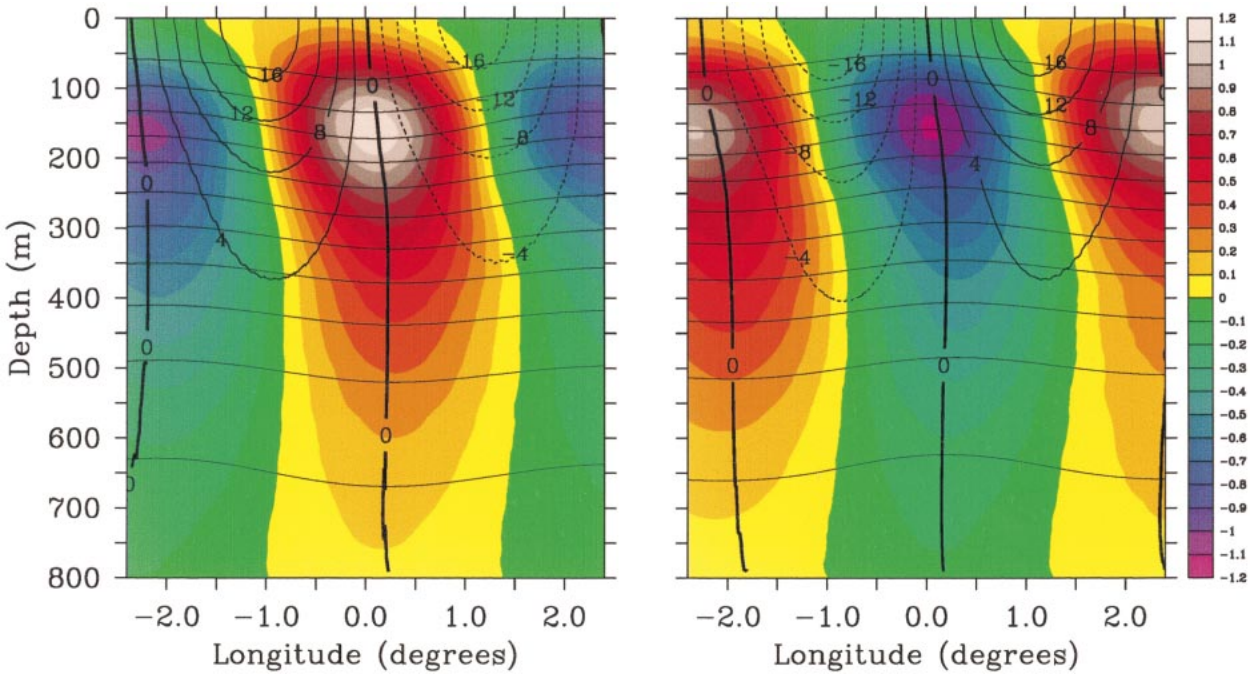

FIG. 5. The composite eddy, showing mean temperature (C.I. = 2°C, warmest contour is 26°C), temperature anomaly (color shading), and geostrophic velocity (cm s^{-1}) based on (left) 192 warm core eddies and (right) 180 cold core eddies.

temperature anomalies and velocity shears are reduced at depth.

The well-determined character of the eddy tilt is demonstrated in Fig. 6. Here, the eddies are further subdivided into four sets: strong (11.3 dyn cm $<$ dyn ht anomaly) and moderate (7.5 $<$ dyn ht anomaly $<$ 11.3), with warm and cold core averages for each of these. Figure 6 shows the eddy center as a function of depth, identified by the location of the maximum or minimum in averaged temperature anomaly. Recall that eddies are aligned in composites based on their dynamic height extrema. There is a striking similarity in slope of the eddy center for each of the four independent composites. An estimate of the standard error in locating each center is shown, based on variability in locating the individual members of each composite. The slope is well determined because of the large number of eddies sampled.

The separation into moderate and strong eddies (Fig. 6) is to display independent composites and to investigate possible effects of spatial aliasing. Because the temperature spectrum is red (Fig. 7a) and XBT profiles are tightly spaced relative to the size of eddies, aliased energy in the eddy band is small compared to resolved energy. Aliasing should be more apparent in the composites of weaker features. The absence of any difference in slope between the strong and moderate composites of Fig. 6 argues that aliasing is not an issue in that calculation. An additional argument is that the vertical coherence of temperature (Fig.7b) drops to near zero at resolved wavelengths shorter than about 300 km, so unresolved features are unlikely to cause systematic noise in composites.

First-mode internal tides are a systematic noise source in the data. In the mid-Pacific, these have wavelength of about 160 km and amplitude of a few meters in thermocline displacement (Dushaw et al. 1995), compared to about 20 m for the composite eddy. These features are resolved by our high-resolution sampling, and are a plausible explanation of the low coherence peak in Fig. 7b (solid line) at about 200 km wavelength. However, with their low energy relative to the eddies and their exclusion by bandpass filtering, they do not bias the composite averages.

The westward shift of eddy centers toward the sea surface is central to the present study. In order for geostrophic eddies to carry heat (i.e., to have net transport in temperature classes), they must tilt, or change phase, in the vertical (see, e.g., Bennett and White 1986). Consider the temperature anomaly field at each depth as the sum of its Fourier components,

$$T'(x, z) = \sum_{n=1}^{N} A_n(z) \sin[k_n x + \phi(z)] + B_n(z) \cos[k_n x + \phi(z)].$$

Assume that the T/S relationship does not change on the scale of the eddy so that density is a function of temperature. Then, from the thermal wind equation,

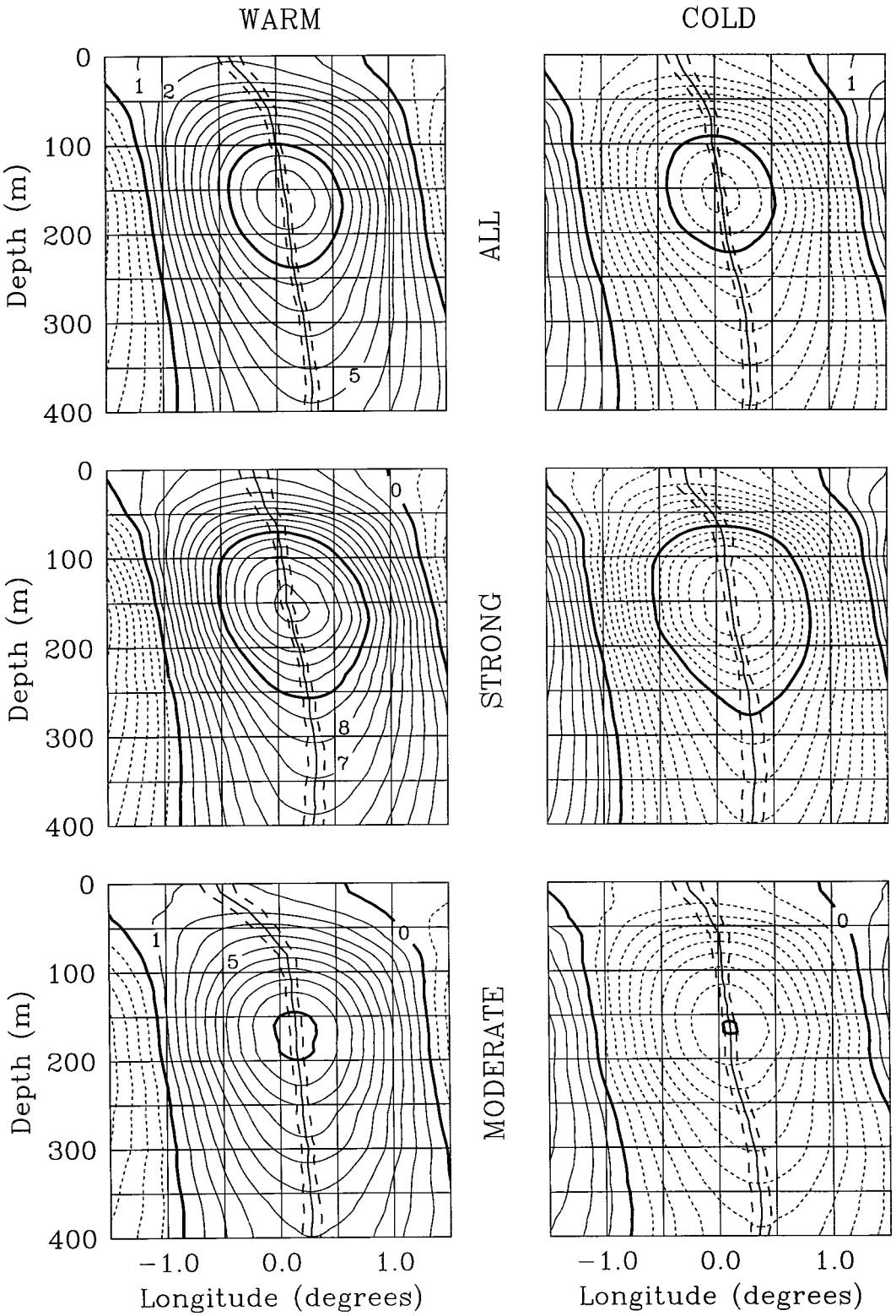

FIG. 6. Location of the center of the composite eddy (solid) and standard error of the location (dashed), superimposed on contours of temperature anomaly (C.I. = 0.1°C). The top row is for all eddies, the middle row for strong eddies and the bottom row for moderate eddies. In each row the left side is the warm core composite and the right side is cold core composite.

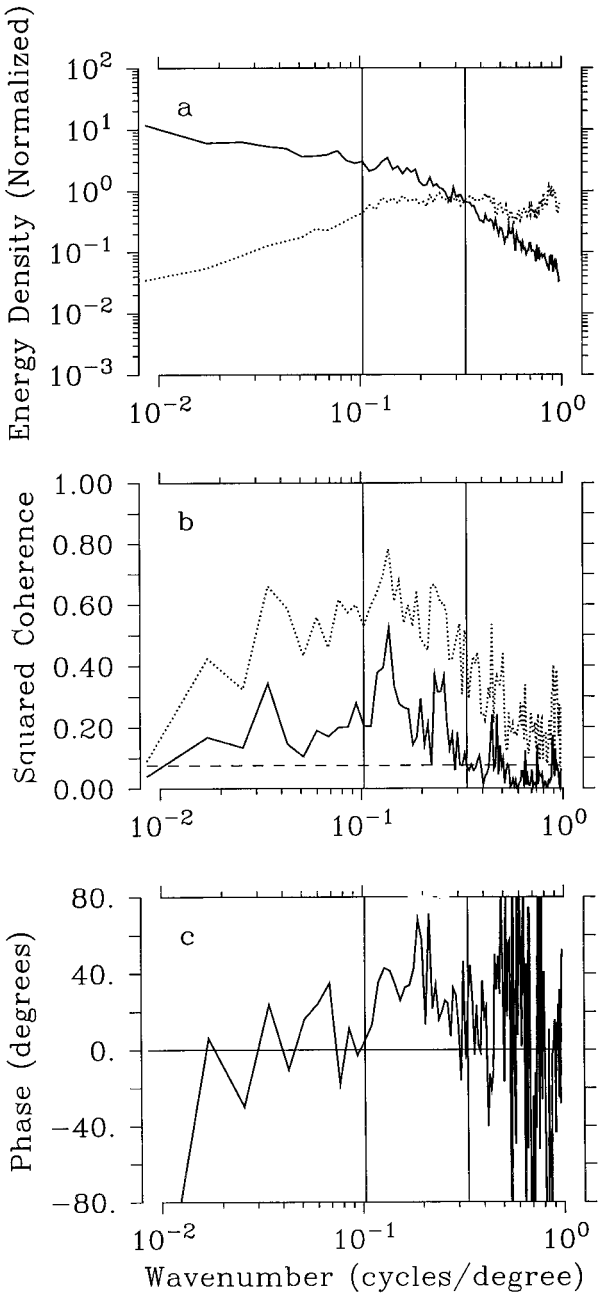

FIG. 7. (a) Wavenumber spectra of temperature (solid) and velocity (dotted) at 100 m. The spectra are normalized to have unit area under both curves. (b) Coherence amplitude squared, of 100-m temperature with 400-m temperature (solid). The dashed line is the 99% significance level (e.g., Goodman 1957). The dotted line is the coherence of 100-m temperature with 100-m velocity. (c) Coherence phase of temperature at 100 m with temperature at 400 m.

$$v' \propto \int_{\text{zref}}^{z} \frac{\partial T'}{\partial x}\, dz$$

$$= \int_{\text{zref}}^{z} \left[\sum_{n=1}^{N} A_n k_n \cos(k_n x + \phi) - B_n k_n \sin(k_n x + \phi) \right] dz.$$

If ϕ is not varying with depth, then velocity and temperature are in quadrature at all depths, and the $v'T'$ product has zero average over an integral number of wavelengths.

A second illustration of the tilt of the eddies is made in the horizontal wavenumber domain. The coherence between 100-m and 400-m temperature is significant for horizontal wavelengths as short as about 300 km (Fig. 7b). The phase difference (Fig. 7c) is consistently positive in the 1000-km to 300-km band chosen for our filter, and is about 30° at 500-km wavelength. This phase difference is consistent with the observed tilt of the composite eddy (Fig. 5).

4. A model eddy

It is instructive to make a functional representation of the composite eddy to demonstrate heat and water mass transport characteristics and their dependencies on eddy tilt and amplitude. For simplicity, a linear thermocline is specified, with a sinusoidal eddy temperature anomaly whose phase varies linearly with depth:

$$T = T_0 + az + b \cos(kx + cz).$$

The constants are chosen for simulation of the composite eddy and the basin-scale transports described in section 5 below. The background temperature gradient is $a = 0.04°\text{C m}^{-1}$. The eddy amplitude, $b = 0.7°\text{C}$, is intermediate between values in the steepest part of the real thermocline (Fig. 5) and those above and below. The wavenumber is $k = 2\pi/5°$ longitude and the phase variation with depth is $c = 2\pi/3200$ m.

The temperature and geostrophic velocity (relative to 400 m, calculated using a constant salinity of 35 psu) of the model eddy are shown in Fig. 8a. Owing to the tilt, the warm center of the eddy has mostly northward velocity, while the cold sidelobes are mostly southward. This gives rise to a $v'T'$ correlation and a heat transport ($\rho C_p v'T'$, Fig. 8b) of 5.36×10^{12} W per eddy.

The eddy's tilt, a westward offset of each isotherm relative to the one below, leads to anomalies in layer thickness that are positive on the eastern (southward velocity) side and negative on the western (northward velocity) side of the eddy. This correlation of layer thickness with velocity results in southward transport of all temperature layers that do not contact the sea surface (Fig. 8c). For sea-surface-contacting layers, the correlation is reversed and transport is strongly northward so that net mass transport over all layers is zero. Altogether, the overturning circulation amounts to 0.30 Sv ($\text{Sv} \equiv 10^6\ \text{m}^3\ \text{s}^{-1}$) per eddy.

The model eddy shown in Fig. 8 is a warm core eddy. A cold core eddy that also slopes toward the west with decreasing depth will have the same transport characteristics as a warm core eddy. In the cold core eddy both the velocity anomalies and the thickness anomalies are reversed—hence the product is unchanged. On the other hand, transport is reversed if the slope is reversed.

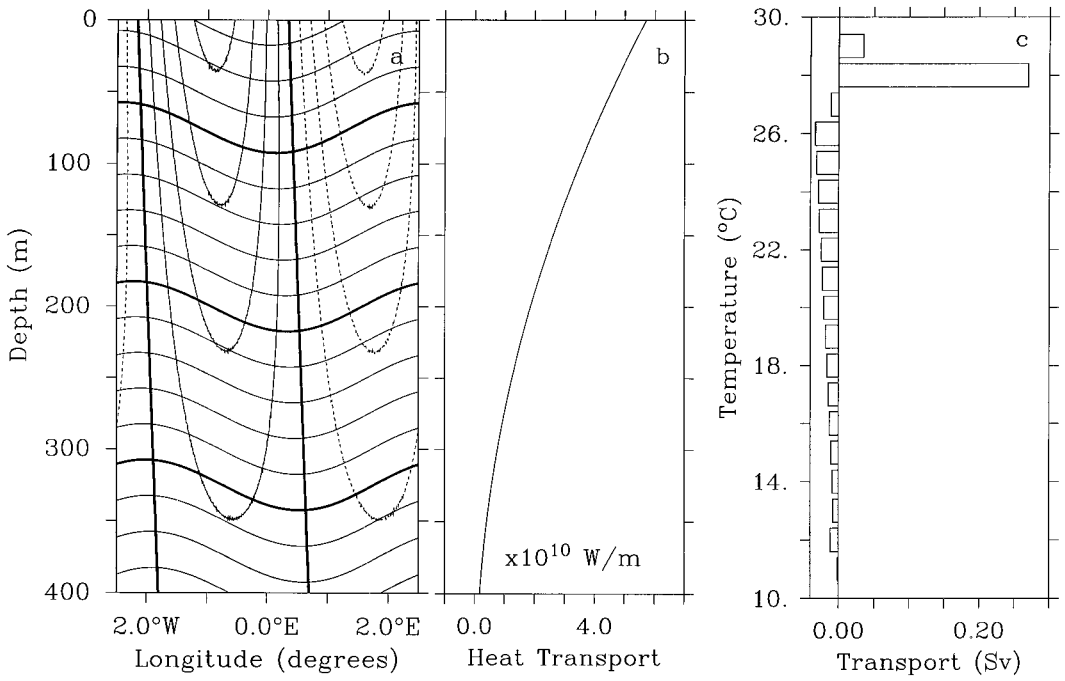

FIG. 8. (a) Temperature (C.I. = 1°C) and geostrophic velocity fields (C.I. = 4 cm s^{-1}) of the model eddy. (b) Heat transport of the model eddy as a function of depth. (c) Transport (Sv) in 1°C temperature bins for the model eddy.

The overturning circulation and heat transport of the model eddy increase approximately linearly with eddy tilt but are quadratic with amplitude because an increase in amplitude increases both the velocity and thickness anomalies. Because of the nonlinearity, the strongest eddies account for a disproportionate fraction of the total transport. Our specific choice of a detection threshold in section 2 (7.5 cm in sea surface height) includes all eddies that substantially impact the transports.

Since there are about 14 eddies along the XBT transect at a given time (Fig. 4b), the net basinwide overturning circulation and heat transport due to eddies is scaled by multiplying model eddy values by 14. This gives 4.2 Sv for the overturning cell and 0.08 pW for the heat transport, which we will see in the next section is reasonable, given the oversimplified structure of the model eddy.

5. Basin-scale eddy transports of heat and thermocline waters

While the characteristics of individual eddies are of interest, it is their basin-integrated effects that are the focus here. In the following, the mean and time-varying components of the basin-integrated eddy fluxes are calculated.

In sections 2 and 3, eddies were identified using a bandpass filter to exclude all but the mesoscale features. Here we adopt a broader definition of eddies—as the deviations from the temporal mean—and will subsequently show below that eddy transports under the broad definition are dominated by the same mesoscale features discussed earlier.

After removing a temporal mean temperature and corresponding geostrophic velocity field from the 30 cruises, deviations (T' and v') from the mean were calculated for each cruise. Eddy transport of temperature is

$$v'T'(x, z, t) = [v(x, z, t) - \overline{v}(x, z)][T(x, z, t) - \overline{T}(x, z)].$$

Eddy heat transport is formed by multiplying $v'T'$ by ρC_p and averaging over time. The eddy heat transport as a function of depth (Fig. 9a), integrated over longitude, is northward in the upper 250 m, with weaker southward transport from 250 to 550 m. Maximum northward transport occurs at 60 to 100 m. Figure 9b illustrates the alongtrack behavior of eddy heat transport. Here the time mean of $v'T'$ is depth-integrated and then integrated from the eastern boundary westward. There is a small southward eddy heat transport near the California coast, then a persistent northward flux over most of the ocean. East of Guam, the change in sign of the slope of the transport integral indicates a reversal to southward heat transport over a narrow region. Standard errors on the variability with depth (Fig. 9a) and with longitude (Fig. 9b) are much smaller than the mean values, indicating statistically robust patterns.

For the 30-cruise mean, the net northward eddy heat transport is 0.086 pW with standard error 0.012. About half occurs east of Guam, with the other half near the Kuroshio. The eddy heat transport is only about 15% of the total heat transport across this transect (Roemmich et al. 2000, submitted to *J. Geophys. Res.*). Nevertheless,

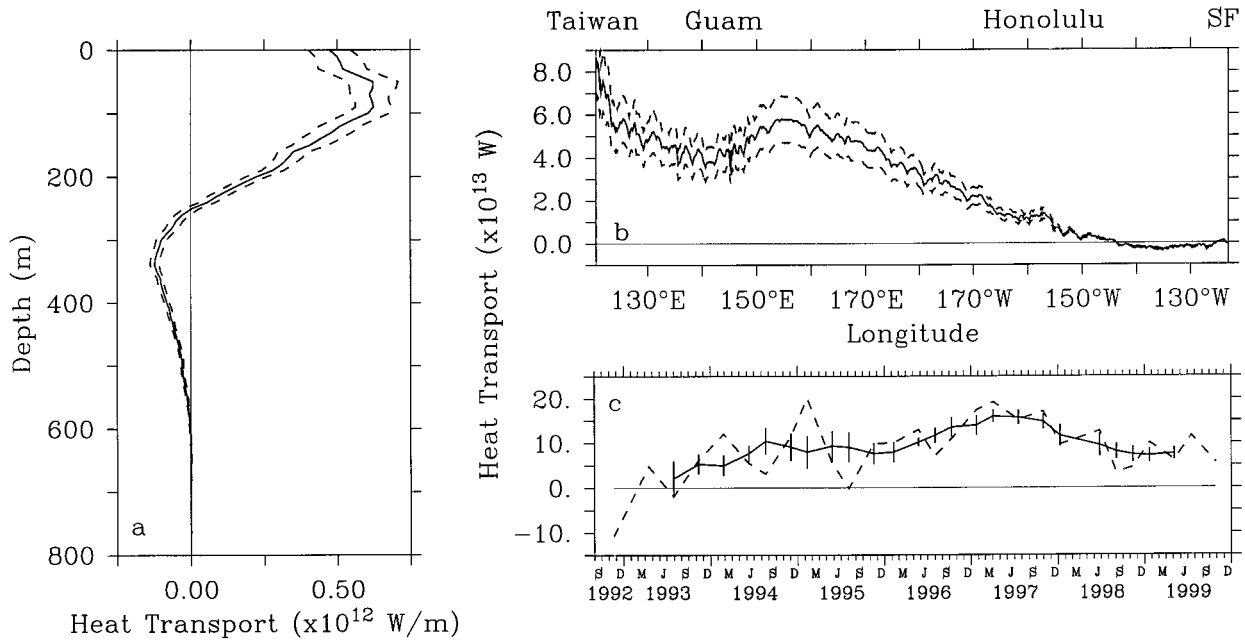

FIG. 9. (a) Heat transport per unit depth (10^{12} W m^{-1}) due to the eddy field, integrated over the length of the XBT transect and averaged in time, with standard error. (b) Integral of eddy heat transport (10^{13} W), 0–800 m, from the eastern boundary westward, averaged in time, with standard error. (c) Time series of eddy heat transport (10^{13} W), 0–800 m and boundary-to-boundary, for the 30 XBT transects (dashed). The solid line shows the five-cruise running mean, with standard error based on variability within each group of five cruises.

the eddy component is persistent and significant. Subsets of the first and last 15 cruises give 0.066 pW ± 0.020 and 0.11 pW ± 0.013, respectively, for the eddy heat transport, indicating significant low-frequency variability.

In order to produce a time series of eddy heat transport, it is necessary to remove the spatial mean of temperature and velocity from each transect rather than removing the temporal mean at each point. That is because the concept of heat transport is only consistent as applied to mass-balanced systems (e.g., Montgomery 1974). Hence, we removed a time mean to describe the heat flux as a function of depth or longitude, and now remove a spatial mean to characterize the variability in time. Since the largest transport anomaly is 6.7 Sv and the largest transect-averaged temperature anomaly is 0.5°C, this adjustment changes individual values of the spatial integral of $\rho C_p v'T'$ by 0.014 pW or less. There is large cruise-to-cruise, and possible low-frequency, variability in the eddy heat transport (Fig. 9c). The interannual pattern of eddy heat transport is shown by applying a five-cruise running mean to the time series, and basing the standard error estimates on variability within each five-cruise group. Values range from about 0.05 pW in early 1994 to 0.15 pW in mid-1997, with standard errors about 0.03 pW.

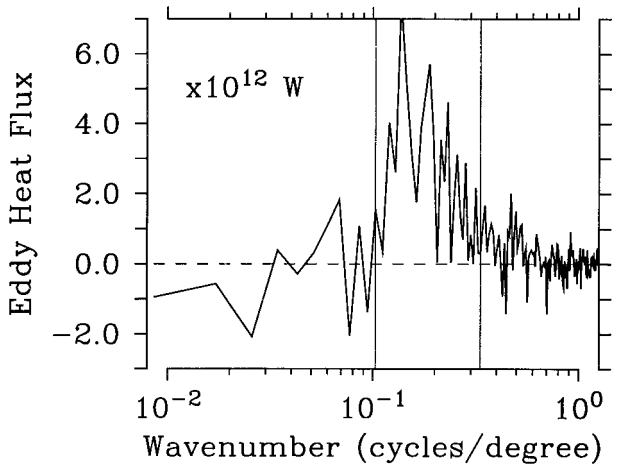

FIG. 10. Horizontal wavenumber cospectrum of v' and T', normalized to show the heat transport (10^{12} w) in each wavenumber estimate.

A cospectrum v' and T', integrated in depth and averaged over all 30 cruises (Fig. 10) reiterates that mesoscale features are responsible for the heat transport. Systematic northward heat transport in the mesoscale band is evident. The sum over wavelengths from 309 to 1002 km gives 0.07 pW, nearly all of the total for $v'T'$.

Our value of 0.086 pW for the mean northward eddy heat transport is much larger than the 0.01 pW value found by Bennett and White (1986) at latitudes of 30°–40°N. Bennett and White (1986) interpolated bimonthly collections of broadscale XBT data onto a 0.5° grid. It is not certain whether the difference is regional or partly due to the use of coarsely resolved XBT data by Bennett

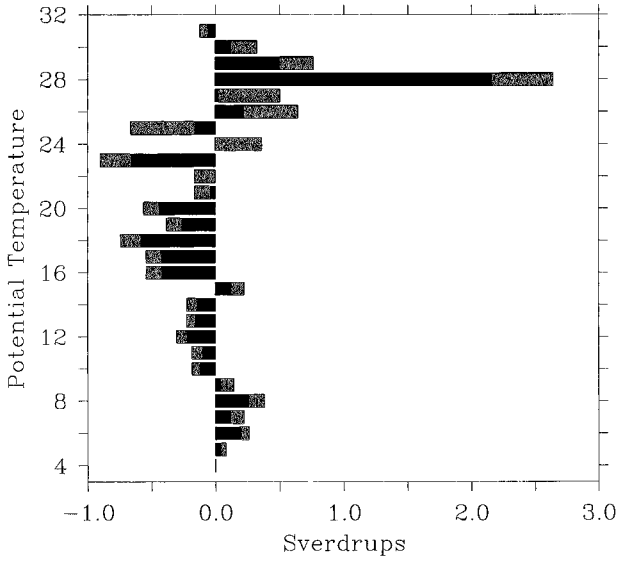

FIG. 11. Mean geostrophic transport in temperature classes due to eddies, from bandpassed data, averaged over 30 transects, with standard error.

and White (1986). Consistent with the present work, they found generally westward phase shifts with decreasing depth for wavelengths around 5°. At shorter wavelengths, they found a reversal in the sign of the eddy heat flux, and that is not observed in the present dataset (Fig. 10).

The net overturning circulation due to eddies is shown in Fig. 11—that is, the mean transport in temperature classes due to v'. As noted previously, there is a correlation of v' with layer thickness, such that thermocline waters tend to be anomalously thick when the velocity is anomalously southward. The resultant net meridional overturning circulation carries about 3.9 Sv of thermocline waters southward (Fig. 11). The 3.9 Sv of southward eddy transport at temperatures from 10° to 26°C is mainly balanced by northward transport of water warmer than 26°C. There is also northward transport of water colder than 10°C due to the deep reversal in eddy tilt. This eddy-driven overturning circulation is the mechanism responsible for eddy heat transport. Figure 11 includes all spatial scales contributing to v'. A bandpassed version (not shown) is similar but less noisy, with net southward transport in the thermocline of 3.0 Sv.

The datasets analyzed here are of short duration for a description of interannual variability. However, since there is low-frequency variability apparent in the eddy field (Figs. 3, 4b, 9c), some investigation is warranted. A time series of the southward geostrophic transport of waters between 10° and 22°C is shown in Fig. 12a (solid line). The 22°C isotherm was chosen to represent the upper bound of the thermocline because the 22°–26°C range is often in the surface layer in the eddy-rich central Pacific. For comparison with the XBT-derived geostrophic transport, the number of eddies detected in the T/P dataset is also shown—as in Fig. 4b but here smoothed by a 90-day running mean. There is some correlation apparent in the two series. Where there is lack of agreement, for example in 1998, we attribute it to variability in the mean tilt of eddies. The 1998 data showed a large number of eddies but with little systematic tilt. The time series in Fig. 12a show similar interannual behavior, with increasing southward transport and numbers of eddies to a peak around the end of 1996. This is consistent with Qiu's (1999) finding that eddy kinetic energy in the T/P dataset increased by 35% between 1993 and 1997 in the region 19°–25°N, 135°E–175°W.

Figure 12b shows the two time series of geostrophic transport and number of eddies, smoothed by five-cruise and 460-day running mean filters respectively, to emphasize interannual variability. Standard error bars on geostrophic transport are based on variability in each five-cruise group. This is an upper bound on errors since there is some resolved annual variability apparent in Fig. 12a. Additionally, for comparison, the eddies were suppressed in a second transport time series (dashed line) by applying the five-cruise running mean separately to the temperature and velocity fields prior to calculating transport in the 10°–22°C range. This eddy suppression has the pronounced effects of both decreasing the mean southward transport in this temperature range, from 13.1 to 10.8 Sv, and of removing the interannual signal. The difference between the total (Fig. 12b, solid) and eddy-suppressed (dashed) transports changes from about 1 Sv in early 1993 to 4 Sv in early 1997. Hence, it appears that the major portion of the interannual variability in thermocline transport is due to fluctuations in the number and/or strength of eddies.

6. Discussion

We have described results from an eddy-resolving XBT transect that crosses the North Pacific at an average latitude of 22°N (Fig. 1). At this latitude there is a maximum in eddy kinetic energy observed by the T/P altimeter (Qiu 1999). This maximum was attributed by Qiu (1999) to baroclinic instability in the vertically sheared region between the eastward subtropical countercurrent (STCC) at the sea surface and the subsurface part of the westward North Equatorial Current (NEC). The STCC is the equatorward part of the C-shaped feature that is characteristic of western subtropical gyres.

Linear stability analyses find that the preferred size of eddies generated by baroclinic instability is 2π times the first-mode Rossby radius of deformation, or about 360 km for the STCC region (Qiu 1999). The eddies we described are somewhat larger, about 500 km (Fig. 5). Once eddies are generated by the baroclinic instability process, it is thought that a nonlinear cascade tends to increase their size until they become large enough to disperse as baroclinic Rossby waves (e.g., Halliwell et

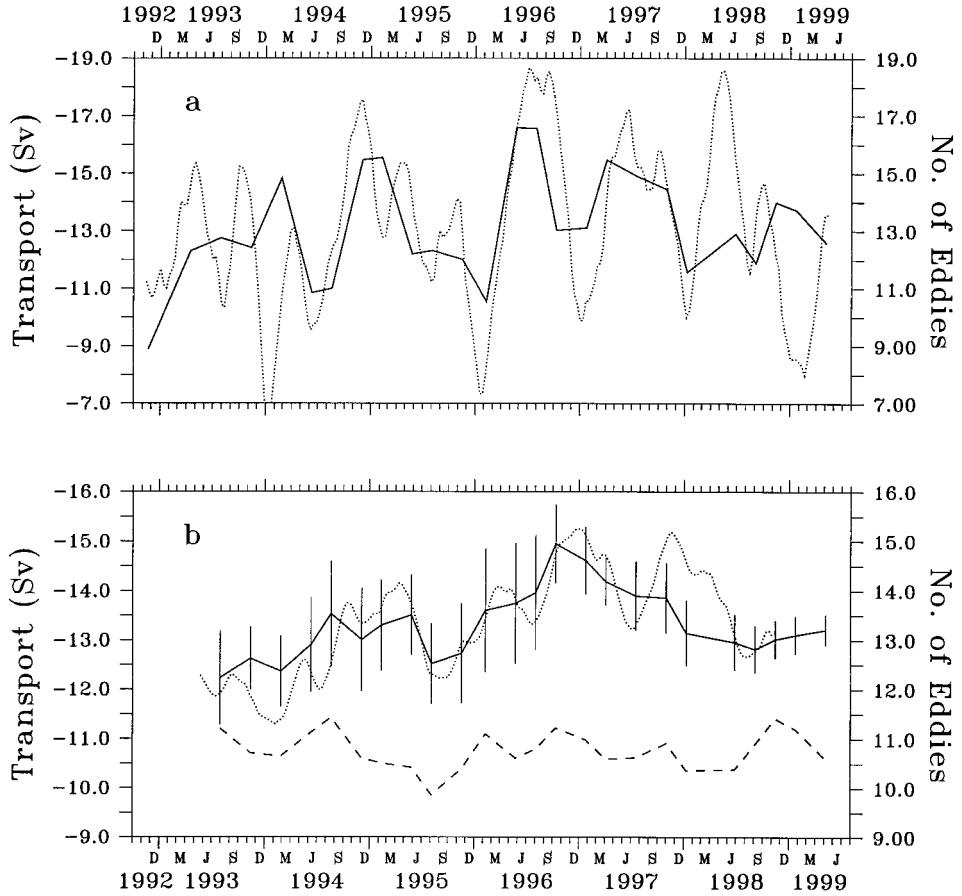

FIG. 12. (a) Time series of geostrophic transport in the range 10°–22°C (solid), number of eddies from T/P, 90-day running mean (dotted). (b) Same as (a) but five-cruise running mean for geostrophic transport (solid), 460-day running mean for T/P data (dotted). Vertical bars show the standard error based on variability in the five-cruise groups. The dashed line is geostrophic transport with the five-cruise running mean applied to temperature and velocity data prior to the transport calculation rather than after.

al. 1994). We are not able to separate the stages of eddy generation and evolution in these observations. In the T/P data along 22°N, it appears that features may propagate all the way from Hawaii (160°W) to the western boundary, a distance of about 8000 km in about 2.5 years (10 cm s^{-1}). Calculations show that the average amplitude of features increases toward the west. However, the size of composite eddies in the west remains at about 500 km, indistinguishable from the central ocean.

The focus of the present work is the transport by eddies of heat and thermocline water masses, and the possible climatic implications of that transport. The slope of the eddies, about 0.8° of longitude toward the west from 400-m depth to the sea surface, is a further indication of the baroclinic instability generation mechanism, and gives rise to the eddy transport characteristics. The eddies produce a net meridional overturning circulation and a northward heat transport of 0.086 pW. The overturning carries about 3.9 Sv of southward transport in the thermocline, mainly balanced by northward flow in the surface layer.

The time-varying characteristics of the eddy population are of particular interest. Variability in the southward transport of thermocline waters was similar to that of the number of eddies (Fig. 12). Eddy heat transport nearly doubled between the first and second half of the sampling period, from 0.066 to 0.11 pW. Over long times, the eddy field may be a major contributor to time variability of northward heat transport. Interannual variability in southward thermocline transport was dominated by change due to eddies, with the eddy transport gradually increasing from about 1 Sv in the range 10°–22°C in early 1993 to 4 Sv in early 1997. If this is representative of longer periods, then time variability in the generation of eddies could be an important cause of interannual-to-decadal climate fluctuations. The implication of an eddy mechanism supplying varying amounts of thermocline waters to the tropical ocean requires further consideration.

This study emphasizes the complementary nature of satellite altimetry and subsurface data. The altimetric dataset yields excellent spatial and temporal coverage of the sea surface. The subsurface temperature (and salinity) profiles are needed to reveal the vertical structure of the phenomena and to provide valuable clues to the underlying dynamics and implications of the combined observations. The complicated nature of the subsurface structure, for example the vertical tilt observed in eddies, cautions against overly simplistic assumptions in modeling and interpretation of sea surface height anomalies.

Acknowledgments. Collection of the XBT/XCTD data was supported by the National Science Foundation through Grants OCE90-04230 and OCE96-32983 as part of the World Ocean Circulation Experiment. The T/P data were kindly provided by the Jet Propulsion Laboratory, and the assistance of L.-L. Fu and A. Hiyashi is gratefully acknowledged. Analysis was supported by the NASA JASON-1 project through JPL Contract 961424. We are grateful for the dedicated efforts of many ship riders in collecting the XBT/XCTD data, under the management of G. Pezzoli. We especially thank Captains Kislinger and Fisher and the officers and crew of S/S *Sea–Land Enterprise* for invaluable assistance to this project. Graphics were produced using FERRET, developed by NOAA/PMEL. Valuable suggestions were made by B. Qiu, R. Davis, D. Stammer, and anonymous reviewers.

REFERENCES

Bennett, A., and W. White, 1986: Eddy heat flux in the subtropical North Pacific. *J. Phys. Oceanogr.,* **16,** 728–740.

Bryden, H., D. Roemmich, and J. Church, 1991: Ocean heat transport cross 24°N in the Pacific. *Deep-Sea Res.,* **38,** 297–324.

Chelton, D., and M. Schlax, 1996. Global observations of oceanic Rossby waves. *Science,* **272,** 234–238.

Deser, C., M. Alexander, and M. Timlin, 1996: Upper-ocean thermal variations in the North Pacific during 1970–91. *J. Climate,* **9,** 1840–1855.

Dushaw, B., B. Comuelle, P. Worcester, B. Howe, and D. Luther, 1995: Barotropic and baroclinic tides in the central North Pacific Ocean determined from long-range reciprocal acoustic transmissions. *J. Phys. Oceanogr.,* **25,** 631–647.

Gilson, J., D. Roemmich, B. Comuelle, and L.-L. Fu, 1998: Relationship of TOPEX/Poseidon altimetric height to steric height and circulation in the North Pacific. *J. Geophys. Res.,* **103,** 27 947–27 965.

Goodman, N., 1957: On the joint estimation of the spectrum, cospectrum and quadrature spectrum of a two-dimensional stationary Gaussian process. Ph.D. thesis, Princeton University, 172 pp.

Gu, D., and S. G. H. Philander, 1997: Interdecadal climate fluctuations that depend upon exchanges between the Tropics and extratropics. *Science,* **275,** 805–807.

Halliwell, G., Jr., G. Peng, and D. Olson, 1994: Stability of the Sargasso Sea subtropical frontal zone. *J. Phys. Oceanogr.,* **24,** 1166–1183.

Montgomery, R., 1974: Comments on ''Seasonal variability of the Florida Current,'' by Niiler and Richardson. *J. Mar. Res.,* **32,** 533–535.

Niiler, P., and M. Hall, 1988: Low-frequency eddy variability at 28°N, 152°W in the eastern North Pacific subtropical gyre. *J. Phys. Oceanogr.,* **18,** 1670–1685.

Qiu, B., 1999: Seasonal eddy field modulation of the North Pacific Subtropical Countercurrent: TOPEX/Poseidon observations and theory. *J. Phys. Oceanogr.,* **29,** 2471–2486.

Sprintall, J., A. Althaus, D. Roemmich, L. Lehmann, B. Comuelle, and R. Bailey, 1996: High-resolution XBT sections in the Pacific and Indian Oceans, 1991–1995. SIO Ref. 96-28, 143 pp.

Stammer, D., 1998: On eddy characteristics, eddy transports, and mean flow properties. *J. Phys. Oceanogr.,* **28,** 727–739.

Wunsch, C., 1999: Where do ocean eddy heat fluxes matter? *J. Geophys. Res.,* **104,** 13 235–13 249.